AD_____

Award Number: DAMD17-00-1-0677

TITLE: MR Elastography System for Breast Cancer Detection

PRINCIPAL INVESTIGATOR: Robert J. Kline-Schoder, Ph.D.

CONTRACTING ORGANIZATION: Creare, Incorporated
Hanover, New Hampshire 03755

REPORT DATE: October 2002

TYPE OF REPORT: Final

PREPARED FOR: U.S. Army Medical Research and Materiel Command
Fort Detrick, Maryland 21702-5012

DISTRIBUTION STATEMENT: Approved for Public Release;
Distribution Unlimited

The views, opinions and/or findings contained in this report are those of the author(s) and should not be construed as an official Department of the Army position, policy or decision unless so designated by other documentation.

REPORT DOCUMENTATION PAGE			*Form Approved* OMB No. 074-0188

Public reporting burden for this collection of information is estimated to average 1 hour per response, including the time for reviewing instructions, searching existing data sources, gathering and maintaining the data needed, and completing and reviewing this collection of information. Send comments regarding this burden estimate or any other aspect of this collection of information, including suggestions for reducing this burden to Washington Headquarters Services, Directorate for Information Operations and Reports, 1215 Jefferson Davis Highway, Suite 1204, Arlington, VA 22202-4302, and to the Office of Management and Budget, Paperwork Reduction Project (0704-0188), Washington, DC 20503

1. AGENCY USE ONLY (Leave blank)	2. REPORT DATE October 2002	3. REPORT TYPE AND DATES COVERED Final (30 Sep 00 – 30 Sep 02)	
4. TITLE AND SUBTITLE MR Elastography System for Breast Cancer Detection		**5. FUNDING NUMBERS** DAMD17-00-1-0677	
6. AUTHOR(S): Robert J. Kline-Schoder, Ph.D.			

7. PERFORMING ORGANIZATION NAME(S) AND ADDRESS(ES) Creare, Incorporated Hanover, New Hampshire 03755 E-Mail: rjk@creare.com	8. PERFORMING ORGANIZATION REPORT NUMBER

9. SPONSORING / MONITORING AGENCY NAME(S) AND ADDRESS(ES) U.S. Army Medical Research and Materiel Command Fort Detrick, Maryland 21702-5012	10. SPONSORING / MONITORING 20030226 100

11. SUPPLEMENTARY NOTES
Original contains color plates: All DTIC reproductions will be in black and white.

12a. DISTRIBUTION / AVAILABILITY STATEMENT Approved for Public Release; Distribution Unlimited	12b. DISTRIBUTION CODE

13. Abstract *(Maximum 200 Words)* *(abstract should contain no proprietary or confidential information)*

Early diagnosis of breast cancer, which is critical for favorable clinical outcomes, is difficult because tumors and healthy tissue respond similarly to X rays and ultrasound. One physical property that clearly distinguishes healthy from cancerous tissue is mechanical stiffness or hardness. Researchers have attempted to combine external mechanical stimulation and Magnetic Resonance Imaging (MRI) to quantitatively measure the Young's modulus of tissue throughout both the breast and the prostate. This technique, Magnetic Resonance Elastography (MRE) has been called "palpation at a distance."

One of the most challenging technical aspects of MRE is the efficient solution of the "inverse problem," i.e., quantitatively determining Young's modulus from MRI-measured tissue displacement data. Creare developed analytical techniques to improve the efficiency and robustness of the inverse problem solution. One technique, which utilizes an incompressible formulation of the tissue equations of motion, an adjoint method for calculating the gradient of the goodness-of-fit metric, and a quasi-Newton minimization algorithm, appears to provide a substantial improvement in efficiency over techniques used previously.

14. SUBJECT TERMS elastography, MRI, inverse problem			15. NUMBER OF PAGES 41
			16. PRICE CODE

17. SECURITY CLASSIFICATION OF REPORT Unclassified	18. SECURITY CLASSIFICATION OF THIS PAGE Unclassified	19. SECURITY CLASSIFICATION OF ABSTRACT Unclassified	20. LIMITATION OF ABSTRACT Unlimited

NSN 7540-01-280-5500

Standard Form 298 (Rev. 2-89)
Prescribed by ANSI Std. Z39-18
298-102

Creare

FOREWORD

Opinions, interpretations, conclusions and recommendations are those of the author and are not necessarily endorsed by the U.S. Army.

( ) Where copyrighted material is quoted, permission has been obtained to use such material.

( ) Where material from documents designated for limited distribution is quoted, permission has been obtained to use the material.
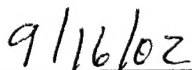
( ) Citations of commercial organizations and trade names in this report do not constitute an official Department of the Army endorsement or approval of the products or services of these organizations.

( ) In conducting research using animals, the investigator(s) adhered to the "Guide for the Care and Use of Laboratory Animals," prepared by the Committee on Care and Use of Laboratory Animals of the Institute of Laboratory Animal Resources, National Research Council (NIH Publication No. 86-23, Revised 1985).

( ) For the protection of human subjects, the investigator(s) adhered to policies of applicable Federal Law 32 CFR 219 and 45 CFR 46.

( ) In conducting research utilizing recombinant DNA technology, the investigator(s) adhered to current guidelines promulgated by the National Institutes of Health.

_____   9/16/02
Principal Investigator's Signature   Date

3

Table of Contents

1 INTRODUCTION

Breast cancer is the most commonly diagnosed cancer in women. Early diagnosis, which is critical for favorable clinical outcomes, is complicated by the difficulty of detecting small tumors. One physical property that clearly distinguishes healthy from cancerous tissue is mechanical stiffness (hardness). For this reason, palpation has long been used for early screening. Researchers have attempted to combine external mechanical stimulation and Magnetic Resonance Imaging (MRI) to quantitatively measure the Young's modulus of tissue throughout the breast (and the prostate as well). This technique, Magnetic Resonance Elastography (MRE) has been called "palpation at a distance." One of the most challenging technical issues of MRE is the solution of the "inverse problem," i.e., robustly and accurately estimating the distribution of Young's modulus from MRI-measured tissue displacement data in a practicable computing time. Addressing this problem was the focus of this project.

Based on understanding developed over the course of this project, as well as recent technical advances made both here and at other institutions, the emphasis placed on different aspects of the scope of work changed somewhat from what was originally anticipated. The following summarizes how we addressed the tasks outlined originally in the proposal:

Task 1: Develop a Finite Element Model for the Behavior of Breast Tissue

Considerably greater work was devoted to this task than originally anticipated. Primarily, this occurred because we determined that much of the work published in the literature, which we initially used as a basis for own study, assumed incorrect (too small) values for the Poisson's ratio. A reduced value improves numerical performance but has the effect of introducing artifacts in the predicted response. For this reason, two sets of finite element codes were developed over the course of the project: a conventional formulation based on compressible, 2-D continuum mechanics, and an innovative model of incompressible behavior. The latter is considered more accurate and also potentially offers substantial gains in computational efficiency. This work is detailed in Sections 2.2, 2.3, and 2.4.

Task 2: Develop Inverse Model

This work proceeded essentially as originally planned, and the effort culminated in an efficient means for solving the inverse problem using an innovative "adjoint" formulation. This work is described in Section 2.5.

Task 3: Develop Hardware for Mechanically Exciting Tissue

Several groups were actively researching MRE during the time period of the project. We determined, based on reviews of the literature, that several approaches were being used to excite tissue in a manner compatible with the requirements of the MRI environment. In particular, piezoelectric actuators and modulated radiation pressure from high-powered ultrasound machines appear to have been quite successful. Based on the success of these other efforts, as well as our findings that more significant needs exist on the analytical front, we concentrated our efforts on Tasks 1 and 2.

2   BODY

2.1   BACKGROUND

Breast cancer is the most commonly diagnosed cancer in women, with a current mortality rate of approximately 23 per 100,000. Early diagnosis, which is critical for favorable clinical outcomes, is complicated by the difficulties associated with detecting small tumors. While mammography is very useful, the X-ray attenuation properties of tumors and normal tissues are similar, often making it difficult to distinguish small tumors from healthy tissue. The same problems afflict ultrasound, since the acoustic impedance of tumors is only slightly different from that of normal tissue.

One physical characteristic that does clearly distinguish healthy from cancerous tissue is mechanical stiffness (hardness). The Young's modulus of breast tumors can be one to two orders of magnitude larger than that of normal tissue (Muthupillai and Ehman, 1996). For this reason, palpation has long been used by both physicians and patients for early screening. However, manual palpation is not very effective for tumors lying deep within the breast and is not quantitative. For these reasons, numerous efforts have been under way over the past decade to combine external mechanical stimulation and various imaging techniques to quantitatively measure the Young's modulus of tissue throughout the breast (and the prostate, as well). This has been termed "palpation at a distance." Because of its inherent sensitivity, most of the current research is focused on exploiting the capabilities of magnetic resonance imaging (MRI), and the overall process is termed magnetic resonance elastography (MRE).

Probably the most challenging technical aspect of MRE is the solution of the inverse problem, i.e., quantitatively inferring Young's modulus from MRI-measured tissue displacement data (Trahey, 2001). Addressing this problem was the focus of the project.

2.1.1   Previous Work on MRE

A number of researchers have investigated use of displacement images to infer the Young's modulus of tissue. Early work focused on utilizing ultrasound images, but much current research employs MRI, which can accurately measure much smaller displacements (less than one micron) with higher resolution than ultrasound.

MRE techniques can be broadly distinguished by whether they employ static or dynamic displacement of the tissue surface. Static techniques measure the change in tissue displacement resulting from a quasi-static push on the outside of the breast, or a sequence of pushes. This method is, in principle, simpler than dynamic methods, but certain mathematical difficulties arise from the use of static displacements. These difficulties appear to have led to the virtual abandonment of this technique (Raghavan and Yagle, 1994; Chenevert et al., 1998; Skovoroda et al., 1995).

Dynamic MRE usually involves the generation of oscillatory motions at the surface of the breast to induce shear waves in the tissue. Because shear waves are strongly attenuated, researchers have also investigated the use of ultrasound to induce shear waves in deep tumors via radiation pressure (Wu et al., 2000). In either case, the motion of the interior of the breast (or phantom) is then measured using MRI, and the elastic modulus is inferred from these measurements.

MRE requires the use of relatively low excitation frequencies since motion at frequencies higher than about 1 kHz cannot be resolved by MRI due to limitations in the maximum modulation rate of the gradient field. Shear waves are used, because even at these low frequencies they have a sufficiently short wavelength to allow the resolution of small features such as tumors. Longitudinal waves have a much faster sound speed, a correspondingly larger wavelength, and thus little resolving power at low frequency.

Three techniques have been used to infer Young's modulus from shear-wave-induced displacement data. Early research efforts employed direct measurements of the wavelength of shear waves at various points in a tissue phantom to determine shear wave speed. From shear wave speed, the modulus can be readily determined (Muthupillai et al., 1995; Manduca et al., 1996). A difficulty of this direct technique is that in real tissue, acoustic waves scatter off tissue inhomogeneities and the scattered waves interfere, generally leading to a very complex pattern of displacements (van Houten et al., 1999). Such a complex pattern does not lend itself to direct measurements of wavelength. To avoid this problem, researchers have turned to physics-based modeling of tissue motion. In one implementation of this method, the equations of motion of the tissue are defined in terms of the known oscillatory boundary conditions and a set of assumed tissue properties (i.e., Young's modulus). These equations are then solved, usually with finite element techniques, and then the calculated displacement patterns are compared to those measured with MRI. The assumed distribution of Young's modulus in the model is then systematically altered and the process repeated until the predicted and measured displacement patterns match to within some tolerance. In another implementation, one derives from the equations of motion, a partial differential equation for the Young's modulus in terms of input tissue displacements (Bishop et al., 2000).

One of the most active groups pursuing physics-based approaches is at Dartmouth College's Medical School and Thayer School of Engineering. They have reported substantial success, but two key problems stand out:

1. The time required to converge the inverse calculations can be impracticably long, even for a relatively coarse mesh on a high-performance workstation. While this has led to the development of so-called subzone techniques and utilization of parallel processing to reduce execution times, this continues to represent a significant practical problem for using MRE in a clinical setting (Van Houten et al., 1999; Van Houten, et al., 2000a, Van Houten et al., 2001).

2. While good results have been reported in numerical simulations, the results in real tissue and in phantoms have been decidedly mixed. This has lead to recent efforts to model transient effects (rather than assuming steady-state), motion in three dimensions (rather than the plane strain approximation used previously), and speculation that viscoelastic behavior may need to be modeled (Van Houten et al., 2000b). Use of these more sophisticated models will further exacerbate the run-time problem.

2.2 GENERAL ASPECTS OF SOLVING THE TISSUE EQUATIONS OF MOTION

Finite element techniques based on physics-based equations of motion can be developed to either solve for the tissue displacements given an assumed set of Young's moduli, or to solve

Greare

directly for the spatially-dependent stiffness by employing a complete set of displacement data. The latter approach is potentially faster but tends to be more sensitive to measurement errors, and our efforts on this project focused on the former scheme.

To develop a solution for the inverse problem using this approach, it is therefore first necessary to develop a numerical model for the tissue displacements given an assumed set of tissue properties, the so-called "forward problem." While a commercial product such as ANSYS can (and was) used for preliminary and scoping analyses as described later, ultimately a customized computer code is needed so that the displacement solution can be integrated with the solution of the inverse problem.

2.2.1 General Form of the Tissue Equations of Motion

For dynamic simulation of vibrations in tissue, finite element codes can be configured to calculate the steady-state amplitude of a damped, linear elastic solid in either three dimensions or in plane strain. Typically the boundary conditions are specified as a harmonically-varying shear displacement along one or more of the edges. In terms of developing a finite-element model, the equations of motion of the nodes of the model can be written:

$$KM\,\overline{u} + \beta KM\,\frac{d\overline{u}}{dt} + MM\,\frac{d^2\overline{u}}{dt^2} = \overline{F} \tag{1}$$

where

$\overline{u}$ = time-dependent displacement vector of the nodes
KM = stiffness matrix (relates displacements to stresses)
MM = mass matrix (defines inertia)
β = Rayleigh damping coefficient that defines the damping ratio in terms of the stiffness matrix
$\overline{F}$ = time-dependent applied external forces

It can be shown that if the desired damping ratio is R, then for an angular excitation frequency ω one should use (Smith and Griffiths, 1998):

$$\beta = \frac{2R}{\varpi} \tag{2}$$

It should be noted that it is also possible to define the damping in terms of the mass matrix, using a slightly different form for the coefficient.

For the case where we assume that a steady-state harmonic excitation at angular rate ω is employed, we define the time-dependent forces and motion in terms of their amplitudes via:

$$\overline{F}(t) = \overline{F}_o e^{i\varpi t} \tag{3}$$

$$\overline{u}(t) = \overline{u}_o e^{i\varpi t} \tag{4}$$

Substituting Equations (3) and (4) into Equation (1), we obtain:

$$(KM + i\beta\varpi KM - \varpi^2 MM)\bar{u}_o = \bar{F}_o \qquad (5)$$

Equation (5) is a time-independent matrix equation for the displacement amplitudes in terms of the amplitudes of the applied forces and an assumed set of tissue properties.

The details of Equation (5) will differ, depending on the precise set of assumptions that are made: compressible versus incompressible, two versus three dimensions, etc. Before considering these details, we first consider general aspects of solving these equations that are common to all of these approaches.

2.2.2 Numerical Solution of the Equations of Motion

It is convenient to write Equation (5) in the standard matrix equation form:

$$A_{ik} x_k = b_i \qquad (6)$$

where A is the (complex) matrix involving the terms in parenthesis in Equation (5), b represents the (real) amplitude of the forces supplied at the surface, and x is the solution vector which is therefore also complex. The Einstein summation convention is used, i.e., a summation is implied on the repeated index k. Physically, the fact that x is complex arises from differences in phase between the displacements at different points within the solid. As evident from Equation (5), the variations in phase are caused by the effects of damping. Careful inspection of the terms in Equation (5) will also reveal that the matrix A in Equation (6) is symmetric.

Actually, one ordinarily does not know the forces applied at the surface of the breast but rather the magnitude of the forced displacements. For this reason, Equation (6) is rewritten in practice so that the surface nodes are forced to have a known vibration amplitude. One way to do this is to replace the associated matrix elements in Equation (6) as follows:

$$A_{ik} = \delta_{ik} \text{ (for all nodal displacements } i \text{ subjected to external forces)} \qquad (7)$$

$$b_i = \text{amplitude of excitation of i}^{\text{th}} \text{ degree-of-freedom} \qquad (8)$$

The terms in b corresponding to non-externally forced nodes are zero.

However, it can be advantageous to use an even simpler scheme in which the on-diagonal element A_{ii} and the corresponding displacement b_i of the equation corresponding to a known displacement u_i are both multiplied by a very large number, so that the external forcing overwhelms the effects of internal forces. This technique preserves the inherent symmetry of the matrix A.

A crucially important aspect of the inverse problem is obtaining an *efficient* solution of the matrix Equation (5) or (6). It should be recognized from the outset that efficiency is more than simply a convenience, since an iterative solution of the inverse problem will usually involve a very large number of solutions of the forward problem. While numerous standard packages exist for efficiently solving sparse, complex, Hermitian matrices, achieving efficiency is complicated in our case because the large matrix A is (at best) symmetric, and therefore is not

Hermitian (i.e., $A \neq A^+$). However, a direct solution scheme is available for equations of the form of (6) that takes advantage of both the sparseness as well as the symmetry of A (Harwell, undated). This is a specialization of the typical LU-decomposition scheme ordinarily used to solve real matrix equations of the form of Equation (6). Aside from raw efficiency, a key advantage of such schemes is that once the matrix A has been decomposed, e.g., factored into lower- and upper-triangular matrices L and U, solutions for different forcing vectors b can be obtained with virtually no additional effort. As demonstrated below, this is very useful for calculating the gradient of functions of the displacements with respect to the input parameters. In any event, the forward problem solution of the symmetric matrix is obtained in about one-eighth the time required for the solution of an asymmetric matrix of the same size.

As part of this project, so-called "mesh-free" techniques were also investigated. When coupled to iterative matrix solution techniques (Smith and Griffiths, 1998), the advantage of this approach is that the complete stiffness and mass matrices MM and KM need never be assembled into memory. This allows very large problems to be solved even when memory is relatively limited. Good results were obtained by solving Equation (6) using a variant of the preconditioned conjugate gradient technique (PCG), namely the biconjugate gradient squared iterative method (Joubert et al., undated). For example, the solution of a 20,000 element grid with 20,000 nodes was obtained in less than about 30 seconds on a 1 GHz personal computer. However, when sufficient memory is available, the iterative techniques cannot compete with the direct approach, so in practice it was found to be better to use the latter.

2.3   THE EQUATIONS OF MOTION OF A COMPRESSIBLE MEDIUM

In this section, we apply the general framework developed in Section 2.2 to the specific case of a linear, compressible medium in the plane strain approximation. We will then investigate some problems associated with the compressibility of the medium.

2.3.1   Development of a Finite Element Code

To support numerical experiments, a solution of Equation (5) was developed for the compressible equations of motion in the plane strain approximation using standard finite element techniques (Smith and Griffiths, 1998). The stiffness and mass matrices were symmetric, allowing the efficient Harwell matrix solution package to be used for the solution.

An exact solution of the displacements is available for the special case of a homogenous rectangular solid, fixed on all but one edge, and subjected to a transverse excitation whose amplitude varies sinusoidally in space across the unfixed edge (Gao, 1995). This solution was compared to the predictions of the Creare finite element code. The latter involved a 10 cm x 10 cm square, modeled using 1 mm x 1 mm 3-node triangular elements. Figure 1 shows the displacement <u>amplitude</u> parallel to the direction of excitation down the midline of the solid. The code results agree reasonably well with the exact solution. It is noteworthy that the value of the damping ratio used in this example problem ($R = 0.1$) is not quite sufficient to prevent some standing waves from developing along the side of the rectangle that is opposite the driven edge.

Of course, the accuracy of the solution is controlled by the fineness of the grid and the fidelity afforded by the various types of elements. Figure 1 utilized a fairly coarse mesh, and more accurate solutions can be obtained by using more elements, quadrilateral elements instead

of 3-node triangles, or triangles with more than 3 nodes. Figure 2 shows the behavior of a snapshot of the displacements at a particular time, i.e., the real part of the complex displacements (not their total amplitude as shown in Figure 1). The cases with a finer mesh (i.e., more nodes) show much better agreement with the exact solution. This experience illustrates an important point: the discretization of the problem domain must be adequate to resolve tissue motion over the wavelengths that will develop for the given excitation frequency. Since the solution time will scale as the cube of the number of grid points, achieving adequate accuracy in a practicable time places a real burden on the analyst. If the analysis is extended to three dimensions, the computational burden can easily become very severe indeed.

2.3.2 The Effect of Poisson's Ratio on Sound Speed

The example calculations with the Creare finite element code mentioned above used prototypical values of the Young's modulus for normal breast tissue and for tumors. However, the value of Poisson's ratio ν in these initial calculations was set to 0.3, a typical value for structural (non-biological) materials. In part, this reflects an initial failure to appreciate the importance of this quantity, which will now be discussed.

To consider what are appropriate values of Poisson's ratio for biological tissues, it is helpful to consider the speed of longitudinal and shear vibrations in tissue. These can be shown to be:

$$c_L^2 = \frac{E(1-\nu)}{\rho(1-2\nu)(1+\nu)} \tag{9}$$

$$c_s^2 = \frac{E}{2\rho(1+\nu)} \tag{10}$$

The value for the Young's modulus E of normal breast tissue is on the order of 10,000 Pa (van Houten et al., [1999] use 8000 Pa). The density of tissue is about that of water, so ρ is approximately 1000 kg/m^3. The speed of longitudinal vibrations c_L is just the sound speed, which is about 1500 m/sec in tissue. Using Equation (9), we can readily determine that Poisson's ratio must be very close to 0.5, so that Equation (9) simplifies to:

$$c_L^2 \cong \frac{E}{3\rho(1-2\nu)} \tag{11}$$

Equation (11) implies that $\nu \sim 0.499999$ if the longitudinal sound speed is 1500 m/sec. In this case, Equation (10) reduces simply to:

$$c_s^2 = \frac{E}{3\rho} \tag{12}$$

It is interesting to note that while the modulus of tissue E varies over a reasonably wide range, the longitudinal sound speed is found to be quite constant, even in tumors (the constancy of the sound speed is why ultrasound is of limited use for detecting cancer) (Duck, 1990).

Equation (11) thus implies that Poisson's ratio must vary <u>slightly</u> as E varies to keep c_L constant. Arguably, therefore, a more appropriate and useful parameterization of tissue would use Young's modulus and longitudinal sound speed rather than Young's modulus and the Poisson's ratio.

2.3.3   Numerical Complications Posed by Modeling Poisson's Ratios Near 0.5

The stiffness matrix KM for compressible media is normally developed from a set of constitutive equations that relate the strains ε to stresses σ (Smith and Griffiths, 1998). In the plane strain approximation, the associated matrix equation is written:

$$\sigma = D\varepsilon \tag{13}$$

where D has terms of the form

$$\frac{v}{1-v} \tag{14}$$

As v approaches 0.5, this matrix, and thus the overall stiffness matrix KM, becomes quite ill-conditioned. Special techniques must be used to obtain a converged solution, which in any case can be difficult. In the limit where the Poisson's ratio becomes 0.5, the material becomes incompressible, the longitudinal sound speed becomes infinite, and a different formulation of the equations of motion becomes necessary. In this formulation, the two displacements are related by the incompressibility condition (conservation of volume), and for this reason an additional variable must be introduced, the hydrostatic pressure. This is discussed further in Section 2.4.

Many finite element codes are incapable of handling the purely incompressible case, and often have convergence difficulties with the nearly-incompressible case as well. Numerical experiments with the Creare-built code showed poor convergence properties as Poisson's ratio was increased to 0.499 and larger. Presumably for the same reason, much of the MRE work reported in the literature utilizes values of 0.45 to 0.49 (Van Houten et al., 2001; Sinkus et al., 2000). At first glance, using 0.49 instead of, say, 0.49999, appears fairly reasonable, until one calculates the sound speeds. At a value of 0.49, for the Young's modulus and density cited earlier, Equation (9) yields:

$$c_L \approx 13 m / \sec \tag{15}$$

This is far less than the actual value of ~1500 m/sec. By contrast, the shear wave speed, given by either of Equations (10) or (12), is about 1.8 m/sec and is insensitive to v.

At an assumed excitation frequency of 200 Hz, in the range typical of MRE applications, the corresponding wavelengths are given by the quotient of the sound speed and the frequency:

$$\lambda_L^* \approx 6.5 cm \tag{16}$$

$$\lambda_s \approx 0.9 cm \tag{17}$$

---

* Artificially reduced Poisson's ratio.

The shear wavelength is comparable to the size of the tumors. As mentioned earlier, achieving small wavelengths at the low frequencies resolvable by MRI is the advantage of using shear waves in the first place. However, the calculated longitudinal wavelength has been made much shorter than the actual value at 200 Hz of about 7 meters. In effect, the use of a Poisson's ratio of 0.49 has made the tissue much more compressible than it actually is, causing the wavelength of longitudinal waves to be much too short.

2.3.4 Errors Caused by Artificial Reductions in Poisson's Ratio

As mentioned previously, the majority of the published work on MRE has involved artificial reductions in Poisson's ratio, just as in the initial Creare analyses, presumably to improve the numerical performance of the inverse algorithm. To investigate the implications of using an artificially reduced value of Poisson's ratio on the calculated tissue behavior, we performed a series of calculations with ANSYS. This code was used rather than the corresponding Creare code since the more advanced formulation of the former more capably handles nearly-incompressible substances. The simulated "breast" in these calculations is a square of dimension 100 mm x 100 mm, excited along the upper edge with a forced displacement whose amplitude varies sinusoidally from zero at the left and right corners to a maximum value of 1 mm in the middle. In all cases, the excitation frequency is 200 Hz, the damping constant β is .00016 (Gao, 1995), and the density ρ is 1000 kg/m^3. The nominal modulus E is 10000 Pa.

Case 1: Correct Poisson's Ratio, Longitudinal Excitation

The first case involves a homogeneous material, and a stiff inclusion representing a tumor has not been included. The Poisson's ratio has been set to a value very close to 0.5 that will yield the proper longitudinal sound speed. The "breast" is excited in the up- and down- direction along the upper edge in an attempt to create longitudinal waves.

A "snapshot" of the calculated displacement amplitudes at a particular time is shown in Figure 3. As noted above, the wavelength of a 200 Hz longitudinal wave in tissue is much larger than the 10 cm maximum dimension of the breast. Thus, no "waves" are seen, just positive amplitude displacements in the y-direction.

Case 2: Correct Poisson's Ratio, Shear Excitation

This is the same as Case 1, except that the breast is excited in the x- (shear) direction. In this case, Figure 4 reveals the production of shear waves with the expected wavelength of about 0.9 cm that are damped fairly quickly with depth. Note that the black box shown in the figure has no significance in this case (the box denotes the location of the inclusion when one is used in Case 4).

Case 3: Artificially Reduced Poisson's Ratio, Longitudinal Excitation

This is the same as Case 1, i.e., there is still no stiff inclusion and the breast is excited in the vertical direction, but in this case a reduced Poisson's ratio of 0.49 is used as in some of the published research. Figure 5 exhibits longitudinal waves with a wavelength of roughly 6.5 cm as expected from Equation (16). The comparison of Figure 5 to the correct behavior shown in Figure 3 clearly illustrates the adverse effects of using too small a value for Poisson's ratio. The

discrepancy would be even worse if still smaller values of v were used (e.g., 0.45), as is seen in the literature.

Case 4: Correct Poisson's Ratio, Stiff Inclusion, Shear-Excitation

This case is similar to Case 2 in that it employs the correct Poisson's ratio. Also, in this case a stiff inclusion is provided at the location of the dark box. The stiffness (increased Young's modulus) of the inclusion leads to an increase in sound speed. The corresponding increase in shear wavelength across the inclusion can be seen in Figure 6. The evident distortions in the wave patterns provide the raw data necessary for an inverse method to estimate the Young's modulus.

As demonstrated by the results shown in Figures 3 through 6, the assumed Poisson's ratio exhibits a profound effect on the displacement patterns. While the use of a reduced value (e.g., 0.49) aids numerical convergence, this cannot be recommended since it gives rise to relatively low longitudinal wave speeds, correspondingly short wavelengths, and substantial distortion of the calculated displacements. An intriguing question is whether this effect may partly explain the artifacts reported in the literature when in vivo data and that from phantoms are used to reconstruct the stiffness. To date, these problems have been attributed to the use of plane strain approximation (rather than 3-D) or to the assumption of linear materials models. If more detailed, 3-D viscoelastic models are needed, this will severely exacerbate the problems of long-running inverse calculations for any future clinical applications, so it would be very useful to resolve this question.

Since the longitudinal wavelengths at the frequencies of interest are much larger than the dimensions of the breast, it appears justified to use a completely incompressible formulation if this will improve numerical performance. This would eliminate the numerical problems associated with modeling nearly-incompressible behavior. Such an approach was previously recommended by Skovoroda et al. (1995). An approximate incompressible formulation is developed in Section 2.4.

2.3.5 Treatment of Damping

Relatively little information exists in the literature on the damping of low frequency shear waves in tissue. What information does exist is often expressed in different ways. To facilitate comparison of these various sources of information and to support the use of different codes that require the damping to be specified in various ways, the following expressions were developed, which are presented here without proof:

a.   Damping ratio R: $\dfrac{\gamma}{2\omega\rho}$

In this expression, γ is the dimensional damping constant (force per unit volume per unit velocity), ω is the angular frequency, and ρ is the density. According to Sinkus et al. (2000), the dimensional damping constant of tissue is typically in the range from 10^5 to 10^6 kg/m^3-sec.

b. Q factor: $\dfrac{\omega\rho}{\gamma}$

Gao (1995) states that a typical value of Q is 4, which is consistent with the R values provided by Sinkus.

c.   Attenuation coefficient: $\alpha = \dfrac{\gamma}{2c_s\rho}$

In this expression, c_s is the shear wave velocity.

d.   Dimensionless attenuation coefficient: $\alpha\lambda_s$

where λ_s is the shear wavelength. Sinkus et al. (2000) state that typical values are 1-6 Np. The relative constancy of the dimensionless attenuation coefficient demonstrates that the attenuation of shear waves increases strongly with frequency.

2.4   APPROXIMATE APPROACH FOR MODELING AN INCOMPRESSIBLE MEDIUM

To achieve good numerical performance without introducing modeling artifacts that will result from reducing Poisson's ratio, an appealing solution is to adopt a fully incompressible formulation, as originally recommended by Skovoroda et al. (1995). More recently, Bishop et al. (2000) have also used this approximation in a direct inversion scheme.

One can motivate this approximation in several ways. Perhaps the simplest way is to apply Snell's law to an incident shear wave propagating at an angle θ_s to the normal of an internal tissue interface:

$$\sin\theta_L = \frac{c_L}{c_s}\sin\theta_s \tag{18}$$

In the limit where the ratio of the longitudinal and shear sound speeds is very large, this expression predicts that an incident shear wave will not produce a reflected or a refracted longitudinal wave in the tissue on either side of the interface. In our case, the speed ratio is roughly 1000, so neglecting longitudinal waves seems quite justified.

In the remainder of this section, we will develop a very efficient, but approximate solution for the incompressible equations of motion.

2.4.1 Derivation of Equations of Motion

The strain and stress tensors, respectively, are defined by Chenevert et al. (1998):

$$\varepsilon_{ij} = \frac{1}{2}(\frac{\partial u_i}{\partial x_j} + \frac{\partial u_j}{\partial x_i}) \tag{19}$$

and

$$\sigma_{ij} = p\delta_{ij} + \frac{2}{3}E\varepsilon_{ij} \tag{20}$$

where the i and j indices specify coordinate axes, and u_i is the displacement in the ith direction. Specializing to the 2-D plane strain approximation, let us denote by u the displacements in the x-direction and use v to refer to displacements in the y-direction. The continuity equation in 2-D is given by:

$$\frac{\partial u}{\partial x} + \frac{\partial v}{\partial y} = 0 \tag{21}$$

A force balance on a small volume of tissue yields the equation of motion in the x-direction:

$$\sum_j \frac{\partial \sigma_{ij}}{\partial x_j} - \gamma \frac{\partial u_i}{\partial t} = \rho \frac{\partial^2 u_i}{\partial t^2} \tag{22}$$

where γ is the (dimensional) damping coefficient and ρ is the density. Substituting Equations (19), (20), and (21) into (22), we obtain after simplifying:

$$\frac{\partial p}{\partial x} + \frac{1}{3}E\left(\frac{\partial^2 u}{\partial x^2} + \frac{\partial^2 u}{\partial y^2}\right) - \gamma \frac{\partial u}{\partial t} - \rho \frac{\partial^2 u}{\partial t^2} = 0 \tag{23}$$

$$\frac{\partial p}{\partial y} + \frac{1}{3}E\left(\frac{\partial^2 v}{\partial x^2} + \frac{\partial^2 v}{\partial y^2}\right) - \gamma \frac{\partial v}{\partial t} - \rho \frac{\partial^2 v}{\partial t^2} = 0 \tag{24}$$

Note that in developing Equations 23 and 24, we have neglected terms involving spatial derivatives of the Young's modulus. The validity of this key simplification will be discussed below.

We can eliminate the pressure by subtracting from the derivative of Equation 23 with respect to y the derivative of Equation 24 with respect to x. Next, in analogy with a very similar concept introduced in incompressible fluid mechanics, we define the "vorticity" by:

$$\xi = \frac{\partial u}{\partial y} - \frac{\partial v}{\partial x} \tag{25}$$

After manipulation, we obtain:

$$\frac{1}{3}E\left(\frac{\partial^2 \xi}{\partial x^2} + \frac{\partial^2 \xi}{\partial y^2}\right) - \gamma \frac{\partial \xi}{\partial t} - \rho \frac{\partial^2 \xi}{\partial t^2} = 0 \tag{26}$$

If necessary, the displacements can be recovered by introducing a function ψ defined as follows:

$$u = \frac{\partial \psi}{\partial y} \tag{27}$$

$$v = -\frac{\partial \psi}{\partial x} \tag{28}$$

The quantity ψ is called the stream function in hydrodynamics, and its use automatically ensures that the continuity Equation (21) is always satisfied. Using the definition Equation (25), the stream function is given by:

$$\xi = \frac{\partial^2 \psi}{\partial x^2} + \frac{\partial^2 \psi}{\partial y^2} \tag{29}$$

Thus, one can solve the incompressible equations of motion using the following sequential procedure:

a. Calculate the vorticity using Equation (26)
b. Calculate the stream function using Equation (29)
c. Differentiate the stream function to yield the displacements via Equations (27) and (28).

We are not especially interested in the displacements per se, but in what they can tell us about the Young's modulus. This being the case, a potentially more efficient procedure would be to base the inverse problem not on the displacements themselves, but on their vorticity. This eliminates the need to solve Equations (29), (27) and (28). To do this one would first obtain estimates for the vorticity distribution by differentiating the MRI-supplied displacement field, possibly smoothing the results afterward to eliminate high frequency measurement noise. Then one would determine a set of Young's moduli that provide the best fit between the experimentally derived vorticities and those calculated by Equation (26). This would be accomplished by inputting to Equation (26) the experimentally measured vorticity values at the boundaries of the breast, and iterating the assumed values of the Young's moduli until a good match is obtained to the interior vorticities. The details of how such an inverse problem can be solved are discussed in Section 2.5.

We note in passing that a somewhat more general derivation of Equation (26) in the absence of damping is provided by Landau and Lifshitz (1986).

2.4.2 Preliminary Assessment of the Vorticity Approach

Let n be the number of grid points used for discretizing the motion of the breast tissue in 2-D. The fundamental equations of motion, Equations (21) involve 3n variables, the pressure and the displacements along both axes. These can be obtained by solving the 3n Equations (21) and (22) (it is also possible to reduce the number of equations to 2n by formally eliminating pressure, as described by Bishop et al., 2000). The prime advantage of the vorticity procedure is that the displacement field can be characterized by solving only n Equations (26). The time required to obtain a solution goes roughly as the cube of the number of equations, so this represents a potential saving in computer time of a factor between eight and twenty-seven, a very significant figure. A somewhat more subtle benefit of the vorticity formulation is that the

underlying equations are symmetric, i.e., are unchanged if the indices i and j are exchanged. As mentioned earlier, efficient solution techniques are available in this case for solving the associated matrix equation. By contrast the 3n set of Equations (21) and (22) are not symmetric and a less efficient solution technique must be used.

However, two potential disadvantages are associated with the vorticity approach. First, the derivatives of the MRI-measured displacement data are used, both as boundary conditions and to serve as the basis of comparison (or "figure-of-merit") used to solve the inverse problem. Differentiation of the data will likely increase the sensitivity to noise in this data. Second, as mentioned above, terms involving the spatial derivatives of the Young's modulus were neglected in the derivation of the Equations (26). As discussed below, these terms may not always be negligible if very steep gradients in tissue stiffness are encountered.

2.4.3   Implementation of the Vorticity Approach

To facilitate experimentation with the vorticity approach, a finite element formulation of Equations (26) was developed in Fortran 90 using the same techniques employed for the compressible displacement-based approach discussed in Section 4. As before, the two-dimensional problem domain was taken to be square (rather than a circle) for simplicity, and 9-node quadrilateral elements were used.

To obtain a solution, a calculation was initially made with ANSYS, which in effect took the place of an MRI machine. These calculations assumed that the upper boundary of the square was excited in the transverse direction by a driving function whose amplitude varied sinusoidally in the x-direction. The other boundaries were assumed to be free. The resulting displacements were differentiated numerically to calculate vorticities. The values of these ANSYS-derived vorticities around the four edges of the square were input as boundary conditions to the Creare code. If MRI data was used, the same procedure would be followed, except that filtering might be necessary to reduce the sensitivity to noise. Utilizing displacement data around the edges allows the simulation to at least partially reflect the edge restraint provided by adjacent tissue layers.

The Creare vorticity code executes very rapidly for a given assumed distribution in Young's modulus. For example, a solution can be obtained on a 100 x 100 grid in only about three seconds using a 1 GHz personal computer. Such a grid allows a planar slice of the simulated breast to be discretized relatively finely, as squares of about 0.1 x 0.1 mm. This is considered adequate for even relatively high frequencies, and is, in fact, considerably finer than many of the simulations reported in the literature.

2.4.4   Comparison of the Vorticity Approach to a Conventional Displacement-Based Scheme

As shown in Figures 7 and 8, very good agreement was obtained between the ANSYS results and those obtained with the Creare code for cases with a spatially constant Young's modulus. It was found that the agreement was improved if the modulus used in the latter was increased by about seven percent over the value assumed in ANSYS; this is attributed to relatively minor differences in numerical technique.

However, larger differences were observed when very strong discontinuities in Young's modulus were introduced to simulate the presence of a tumor. In the calculations discussed below, the tumor was represented by an area that has a Young's modulus that is ten times that of healthy tissue (100 kPa versus the nominal stiffness of 10 kPa). The location of the tumor was in the upper right-hand corner of the problem domain, i.e. at:

$$0.02m \leq x \leq .03m$$

$$0.02m \leq y \leq .03m$$

Figures 9 and 10 show the vorticities calculated by ANSYS and the Creare code for this case. While these do not appear too different, differences can be seen in the detailed behavior around the inclusion. To see this even more clearly, consider a similar case where the excitation frequency is reduced from 200 Hz to 50 Hz. The overall vorticities, Figures 11 and 12, again appear qualitatively similar. However, Figure 13 shows the vorticity values along a vertical path through the simulated tumor. Note that a sharp discontinuity occurs at the bottom edge of the tumor where a sudden, large change in Young's modulus is experienced. A smaller discontinuity occurs at the top. These jumps in vorticity can be shown to result from terms involving the second spatial derivatives of the Young's modulus that were neglected in the derivation of Equations (26). While qualitatively similar, the vorticities calculated by the Creare code along the same path have no such discontinuities. The differences in vorticity near the excited edge (y=.05 cm) are believed to be caused by differences in reflections at the tumor.

For a similar problem in which the (again discontinuous) change in Young's modulus is assumed to be "only" a factor of 2 and the frequency is restored to the nominal value of 200 Hz, the "vorticity jump" calculated by ANSYS is much less pronounced, as shown on an expanded scale in Figure 14. Also, the results of the two codes in this case agree fairly well. The vorticity jump would be smaller still if the tissue properties were allowed to vary more smoothly than the artificial step changes we have assumed. It remains to be seen whether vorticity jumps in actual tissue are so large as to compromise our ability to estimate Young's modulus using this method. If the jumps are indeed that dramatic, we can speculate that the vorticity concept could provide a means to process raw displacement data and detect sudden changes in Young's modulus without solving an inverse problem at all.

2.4.5 Discussion

An extremely efficient approximate solution technique for the tissue equations of motion was developed. Using a relatively modest 1 GHz personal computer, a solution can be obtained on a 100 x 100 planar grid in only about three seconds. Further increases in execution speed are possible.

Two key assumptions contribute to the efficiency of this solution. First, the tissue is assumed to be incompressible. This implicitly neglects the existence of longitudinal waves, which is justified on the basis of their relatively high propagation velocities and long wavelengths. Second, the Young's modulus is assumed to vary sufficiently so slowly that its higher order spatial derivatives can be neglected.

Further work is necessary to validate whether the vorticity approximation can be used when analyzing actual tissue displacements. If the vorticities calculated from MRI displacement data exhibit large, discontinuous jumps, this may invalidate the use of vorticity for quantitatively modeling tissue response. However, in this case, the vorticity concept could still be useful since the vorticities calculated from displacement data may provide a direct and even more efficient means to locate regions where tissue stiffness is rapidly varying.

2.5   SOLUTION OF THE INVERSE PROBLEM

2.5.1   Overview

A conventional scheme for solving the inverse problem is to minimize a figure of merit of the form:

$$J = \sum_{i=1,..n} (u_i - u_i^o)^2 + (v_i - v_i^o)^2 \tag{30}$$

In Equation (30), u and v denote the x- and y-direction displacements at each of the n nodes of a plane strain displacement model at some specified time in their oscillatory cycle. The superscript "o" denotes displacements obtained from measured MRI data (which can come from an actual MRI or from a finite element simulation). The lack of a superscript denotes code-calculated displacements based on the current estimate for Young's modulus at each node. The same expression would be used for a 3-D analysis or one based on vorticity, the only difference being the number of terms included in the sum.

The Dartmouth group determines Young's modulus by minimizing J using a well-known technique known as the Levenberg-Marquardt algorithm (Press et al., 1986). This requires the estimation of the Hessian matrix associated with J, which in turn requires the calculation of terms such as:

$$\frac{\partial u_i}{\partial E_k} \text{ and } \frac{\partial v_i}{\partial E_k} \quad i=1,...n; k=1,...p \tag{31}$$

where E_k denotes the Young's modulus of the kth element in the finite element model. If there are n nodes and p elements in the model, the calculation of the nodal displacements requires a time proportional to roughly n^3. However, the calculation of the terms (31) requires a time that is p times longer than this, which for low order elements (for which p is roughly equal to n) is on the order of n^4. This is a significant disadvantage as the number of elements and nodes grows unless the calculation of these quantities makes convergence to the proper Young's modulus distribution much more rapid.

Since the time required to calculate the terms in the approximate Hessian matrix is very long, we instead investigated the use of a quasi-Newton method, specifically the Boyden-Fletcher-Goldfarb-Shanno (BFGS) algorithm (Press et al., 1986). While this method is likely to require more iterations to converge than Levenberg-Marquardt, BFGS requires the calculation of only the gradient of the figure-of-merit, i.e., the terms:

$$\frac{\partial J}{\partial E_k} \qquad k=1,\ldots p \tag{32}$$

To facilitate use of this technique, we developed an algorithm that very efficiently calculates the terms of the gradient.

2.5.2 Calculation of the Gradient of the Figure-of-Merit

As discussed previously, given a set of measured (or simulated) displacement or vorticity data, one adjusts the assumed Young's moduli to make the calculated values agree with the measured quantities. This can be formulated as an optimization problem, in which a measure of the disagreement, Equation (30), is minimized.

Most efficient and robust techniques for minimizing figure-of-merit functions of the form of Equation (30) require information on the change in the predicted displacements caused by a small change in input parameters. For example, the Levenberg-Marquardt technique requires extensive information that is time-consuming to calculate, i.e., the terms shown in Equation (31). The BFGS technique requires less gradient information, but it is still critical to develop this information in an efficient manner. For example, the crudest approach to calculate the gradient terms shown in Equation (32) would involve making a small change in a single modulus E_k and then recalculating the entire displacement solution. Repeating this process p times to calculate all such terms would again require a time on the order of p times n^3, or roughly n^4. In other words, this brute-force process would require the same length of time as the Levenburg-Marquardt method.

Note that the brute-force technique calculates the change in each displacement or vorticity caused by a change in the input Young's moduli. Since we then sum over these displacements to calculate the figure-of-merit J, we see that the brute-force technique calculates much more information than we really need for BFGS. A better scheme is to use an adjoint technique that efficiently calculates only the needed information (Kenton, 1981). If we have a set of algebraic equations of the form:

$$0 = g_i(x) \tag{33}$$

together with a single figure-of-merit $J(x)$, one defines an adjoint x^+ associated with each variable x by constructing the following equations:

$$0 = \sum_k \frac{\partial g_k}{\partial x_i} x_k^+ + \frac{\partial J}{\partial x_i} \tag{34}$$

After the terms x^+ have been calculated using Equation (34), the terms of Equation (32) can be obtained very simply by calculating the following sums:

$$\frac{\partial J}{\partial E_k} = \sum_i \frac{\partial g_i}{\partial E_k} x_i^+ \tag{35}$$

◎reare

In our case, Equations (33) are linear, and the matrix terms in Equation (34) put into the standard form of Equation (6) are of the form:

$$A_{ik} = \frac{\partial g_k}{\partial x_i} = KM_{ki} + i\beta\varpi KM_{ki} - \varpi^2 MM_{ki} \tag{36}$$

When the stiffness and mass matrices KM and MM are symmetric, and when this symmetry is not destroyed by using an injudicious formulation of the boundary conditions, the matrix A' used to solve for the adjoints is the same as the matrix A used to solve for the displacements or the vorticities.

This symmetry offers the potential for a still larger savings in computation time, if sufficient memory is available to use direct sparse matrix techniques rather than an iterative scheme such as PCG. If we use such a direct matrix solution technique, we will manipulate A in some fashion (e.g., decompose it into upper- and lower-diagonal matrices) that will then allow the matrix equation to be readily solved. The time-consuming part of the solution process is the matrix manipulation step, which takes a time on the order of the cube of the rank, i.e., in this case n^3. The subsequent "back-substitution" process needed to obtain the solution x for a given b takes, by contrast, only a time on the order of n^2. Thus, direct methods are very appealing when used with the BFGS algorithm: after the matrix A has been manipulated to obtain a solution of the forward problem, the adjoints can be obtained with the same matrix decomposition in essentially negligible additional time. The gradient terms are then obtained trivially using Equation (35).

2.5.3 Demonstration Calculation of Determining Young's Modulus From Data

To experiment with the inverse algorithm, both the compressible, displacement-based finite element code and the incompressible vorticity code were augmented to calculate the gradient terms using the adjoint method. After doing this, it was first confirmed that the change in figure-of-merit caused by a change in one or more of the Young's moduli calculated using brute-force techniques was the same as predicted by the adjoint method. The gradient information was then used to minimize the figure-of-merit Equation (30). We tried several algorithms to achieve this, and the best results were obtained using a commercially-available implementation of the BFGS algorithm (IMSL, 1994). Figure 15 shows the relative rate at which the figure-of-merit converged in a typical problem (a value of zero for the figure-of-merit implies perfect convergence).

Figure 16 shows the Young's modulus obtained from computer-generated MRI displacement vorticity "data." Computer-generated data were obtained by merely running the finite element code on a 100 x 100 grid for a specified Young's modulus distribution, in this case a uniform distribution with a value of 10 kPa except for a square "tumor" of value 100 kPa in the upper-right-hand corner. The minimization procedure then begins with a uniform (and incorrect) Young's modulus assumption, and iterates until the desired accuracy is obtained. As can be seen in Figure 16, the algorithm does an excellent job inferring Young's modulus from the computer-generated data. This simulation required approximately 10 minutes of computer time on a 1000 MHz personal computer. While several possibilities exist for further increasing the speed

of this procedure, the relatively short time required to obtain good convergence is a direct consequence of:

a. Use of the vorticity formulation, which results in a greatly reduced number of equations for a given discretization.

b. The use of a boundary condition formulation that results in a symmetric A matrix.

c. Exploiting the adjoint formulation to very efficiently calculate the gradient of the figure of merit.

As shown in Figure 17, similar success was also obtained using a displacement-based formulation (with an artificially reduced Poisson's ratio). Should the vorticity scheme prove too inaccurate when applied to actual MRI-measured tissue displacements, this success indicates that an incompressible version of the displacement model such as that used by Bishop et al. (2000) should converge just as well as the vorticity scheme, but in a longer time. Nevertheless, even in this case the efficiency advantages of using adjoints should permit convergence in a much shorter period than is required by other techniques.

Acknowledging the difficulties implicit in matching the vorticity model to ANSYS results when sharp discontinuities in assumed stiffness are present, a final inverse problem was run in which the ANSYS results were input to the vorticity approach. The reconstructed Young's modulus distribution is shown in Figure 18 (note that the figure actually shows "smoothed" data, in which each modulus value was averaged with its nearest neighbors to suppress high frequency oscillations that occur near the vorticity jumps). The results are considered surprisingly good, and the tumor can clearly be discerned. This suggests that even with its simplifying assumptions, the vorticity approach may still yield acceptable results when applied to real data.

One important detail of the inverse algorithm should be explained. Initial numerical experiments resulted in a much poorer reconstruction of the Young's modulus than is shown in Figures 16 and 17. Inevitably, we found that the method converged on a solution that involved non-physical (negative) Young's moduli adjacent to the "tumor." Further, the calculated Young's moduli inside the tumor boundary compensated for this and were too large. Other numerical artifacts involving negative Young's moduli also sometimes appeared near the boundary of the simulated breast. To solve these problems without instituting the full complication of a constrained minimization approach, the Young's moduli were mapped to a new variable α, and convergence was obtained on α. The mapping used:

$$E_k = E_{\min} + \alpha_k^{\,2} \tag{37}$$

which guarantees that the Young's modulus will be larger than some physically-based minimum value E_{min}. This modification to the algorithm proved very beneficial.

In these demonstration calculations, the damping was assumed known. When applied to real data, the damping may well vary across a cross section of the breast, although there is little in the literature to imply how much variation should be expected. In any event, simultaneously

Greare

solving for unknown damping coefficients along with the Young's moduli should not lead to any additional complications. In particular, the gradient of the figure-of-merit with respect to the damping is obtained from an expression of the form of Equation (35), using the same values for the adjoint functions as are used to calculate the gradient with respect to the Young's moduli.

3 KEY ACCOMPLISHMENTS

- An adjoint method developed on this project provides an extremely efficient technique for calculating the gradient of the goodness-of-fit measure that is the basis of the inverse algorithm.

- Combining the adjoint method with the BFGS algorithm provides an efficient means for calculating tissue stiffness from MRI displacement data.

- Much of the experience with Magnetic Resonance Elastography previously reported in the literature has utilized an incorrect value of Poisson's ratio.

- Use of an incorrect Poisson's ratio leads to a drastic underprediction of the longitudinal acoustic wavelength, which in turn can be expected to cause artifacts in the reconstructed hardness values.

- An incompressible tissue model developed under this project provides an extremely efficient method for calculating tissue displacements.

- Demonstration of the speed and accuracy of our incompressible tissue model linked to our inverse problem solution method using 2-D computer-generated data.

4 REPORTABLE OUTCOMES

- Era of Hope Poster Presentation for Department of Defense Breast Cancer Research Program Meeting, September 25, 2002, Orlando, FL. (See Abstract at end of Appendices section.)

- Grant entitled "MR Elastography for Breast Cancer Detection," submitted to NIH/SBIR July 25, 2002.

5 CONCLUSIONS

In this report, we have developed an efficient method for determining Young's modulus from tissue displacement data. The method is based on minimizing a figure-of-merit that indicates how closely the experimental measurements match a model of the tissue response. One hallmark of this method is the use of an adjoint technique for calculating the gradient of the figure-of-merit with respect to the unknown quantities (i.e., Young's modulus and, perhaps, damping) in a time that is negligible compared to the solution of the tissue equations of motion.

Use of artificially reduced values for the Poisson's ratio, as is often done, was found to introduce severe artifacts into the calculated displacements. A better approach is to assume completely incompressible behavior.

Very fast convergence of the calculated Young's modulus distribution was obtained with simulated displacement data by using a "vorticity" scheme that models 2-D incompressible behavior using a greatly reduced number of equations. Further work is needed to determine whether the approximations inherent in this approach will be sufficiently accurate when applied to actual *in vivo* data.

6   REFERENCES

J. Bishop, A. Samani, J. Sciarretta, D. B. Plewes, Two-Dimensional MR Elastography With Linear Inversion Reconstruction: Methodology and Noise Analysis, *Phys. Med. Biol.* 45, 2081–2091 (2000).

T. L., Chenevert, A. R. Skovoroda, M. O'Donnell, S. Y. Emelianov, Elasticity Reconstructive Imaging via Stimulated Echo MRI, *Magnetic Resonance In Medicine* 39 (1998).

F. A. Duck, *Physical Properties of Tissue*, Academic Press (1990).

L. Gao, Sonoelastography: Theory and Experiment Development, Ph.D. thesis (University of Rochester, 1995).

Harwell Sparse Matrix Package, procedure ME47 (undated).

W. D. Joubert, Y. Shen, S. Swift, Getting Started with PCG, Version 1.0 (Los Alamos National Laboratory, undated).

M. A. Kenton, A General Sensitivity Theory for Simulations of Nonlinear, Time-Dependent Systems, Cornell University Reactor Laboratory, report CURL-58 (January 1981).

L. D. Landau, E. M. Lifshitz, *Theory of Elasticity*, New York, Pergamon Press (1986).

A. Manduca, R. Muthupillai, P. J. Rossman, J. F. Greenleaf, R. L. Ehman, Image Processing for Magnetic Resonance Elastography, SPIE 2710, 616–623 (1996).

R. Muthupillai, R. L. Ehman, R.L., Magnetic Resonance Elastography, *Nature* 2, 5 (May 1996).

R. Muthupillai, D. J. Lomas, P. J. Rossman, J. F. Greenleaf, A. Manduca, R. L. Ehman, Magnetic Resonance Elastography by Direct Visualization of Propagating Acoustic Strain Waves, *Science* 269 (September 29, 1995).

W. H. Press, B. P. Flannery, S. A. Teukolsky, W. T. Vetterling, *Numerical Recipes*, Cambridge University Press (1986).

K. R. Raghavan, A. E. Yagle, Forward and Inverse Problems in Elasticity Imaging of Soft Tissues, *IEEE Trans. Nuclear Science* 41, 4 (August 1994).

R. Sinkus, J. Lorenzen, D. Schrader, M. Lorenzen, M. Dargatz, D. Holz, High-Resolution Tensor MR Elastography for Breast Tumor Detection, *Phys. Med. Biol.*, 45, 1649–1664 (2000).

A. R. Skovoroda, S. Y. Emelianov, M. O'Donnell, Tissue Elasticity Reconstruction Based on Ultrasonic Displacement and Strain Images, *IEEE Transactions on Ultrasonics, Ferroelectrics, and Frequency Control*, 42, 4 (July 1995).

I. M. Smith, D. V. Griffiths, *Programming the Finite Element Method*, Third Edition, John Wiley (April 1998).

G. Trahey, remarks made during discussion of paper 4325-14, K. Nightingale, M-S Soo, R. Nightingale, M. Palmeri, G. Trahey, Investigation of Real-time Remote Palpation Imaging, Medical Imaging 2001, SPIE, San Diego (2001).

E. E. W. Van Houten, K. K. Paulsen, M. I. Miga, F. E. Kennedy, J. B. Weaver, An Overlapping Subzone Technique for MR-Based Elastic Property Reconstruction, *Magnetic Resonance in Medicine* 42, 779–786 (1999).

E. E. W. Van Houten, K. D. Paulsen, M. I. Miga, F. E. Kennedy, J. B. Weaver, A Subzone Based Nonlinear Inversion Scheme for Viscoelastic Tissue Properties, Medical Imaging 2000: Image Processing, Proc. SPIE Vol. 3979 (2000b).

E. E. W. Van Houten, J. B. Weaver, M. I. Miga, F. E. Kennedy, K. D. Paulsen, Elasticity Reconstruction from Experimental MR Displacement Data: Initial Experience with an Overlapping Subzone Finite Element Inversion Process, *Med. Phys.* 27, 1 (January 2000a).

E. E. W. Van Houten, M. I. Miga, J. B. Weaver, F. E. Kennedy, K. D. Paulsen, Three-Dimensional Subzone-Based Reconstruction Algorithm for MR Elastography, *Mag. Res. In Med.,* 45, 827–837 (2001).

T. Wu, J. P. Felmlee, J. F. Greenleaf, S. J. Riederer, R. L. Ehman, MR Imaging of Shear Waves Generated by Focused Ultrasound, *Magnetic Resonance in Medicine* 43, 111–115 (2000).

Creare

7   PERSONNEL WHO RECEIVED PAY FROM RESEARCH EFFORT

Affleck, Wayde H.—Engineer
Berg, Joel L.—Engineer
Cook, Jessica L.—Library Assistant
Copps, Dale G.—Library Manager
Gallagher, Arthur C.—Contracts Manager
Kenton, Marc A.—Engineer
Kline-Schoder, Robert J.—Principal Engineer
Kynor, David B.—Engineer
Murray, Lynne A.—Administrative Secretary
Robinson, Frances E.—Administrative Secretary
Rothe, Paul H.—Principal Engineer
Sorensen, Paul H.—Engineer
Wilson, John P.—Engineer

8   APPENDICES
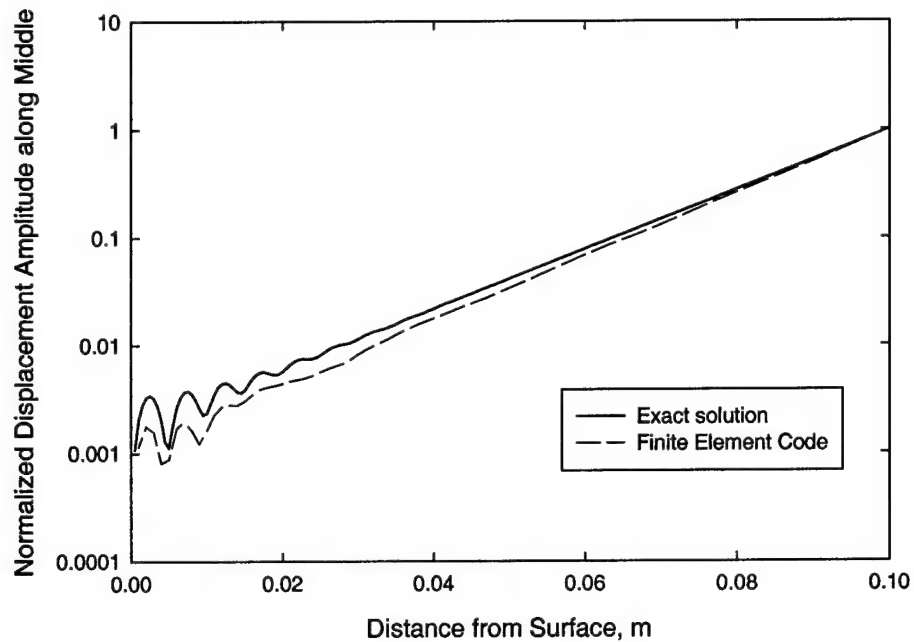
Figure 1. Comparison of Finite Element Code Predictions of the Logarithm of the Displacement Amplitude to the Logarithm of the Displacement Amplitude for the Exact Solution. These data show that our finite element code closely matches the exact solution for the analyzed configuration.
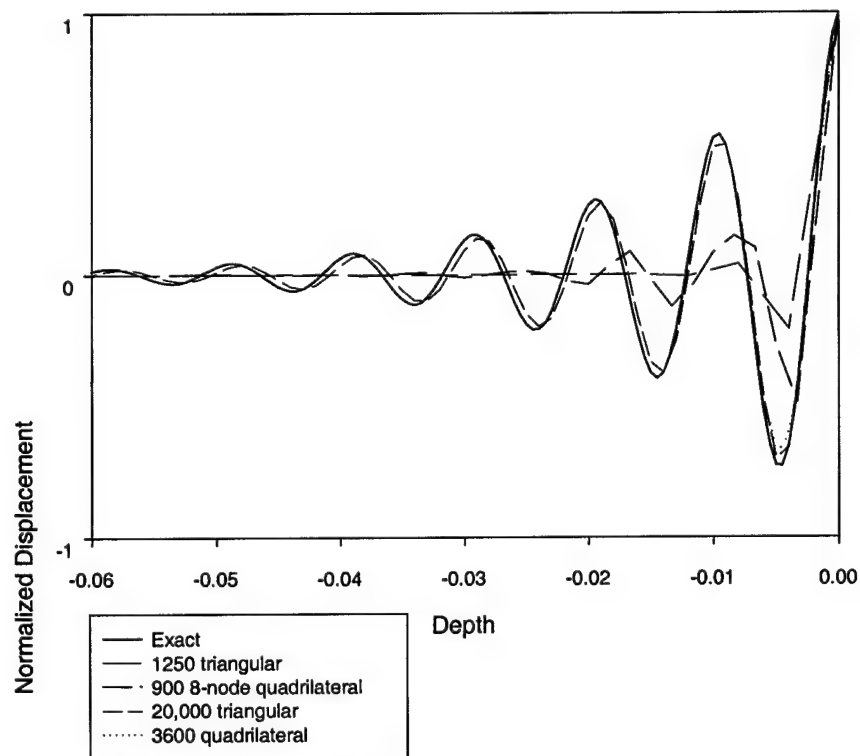
Figure 2. Instantaneous Displacements Versus Depth for Various Meshing Schemes. These data show the effect of model order on the match to the exact solution. For this model, 3600 quadrilateral elements or 20,000 triangular elements yield good model accuracy.

31

```
ANSYS 5.7
MAY 22 2001
08:56:26
NODAL SOLUTION
STEP=1
SUB =1
FREQ=200
UY          (AVG)
RSYS=0
PowerGraphics
EFACET=1
AVRES=Mat
DMX =.657E-03
SMN =-.854E-04
SMX =.500E-03
     -.854E-04
     -.510E-04
     -.165E-04
      .179E-04
      .523E-04
      .867E-04
      .121E-03
      .156E-03
      .190E-03
      .224E-03
      .259E-03
      .293E-03
      .328E-03
      .362E-03
      .397E-03
      .431E-03
      .465E-03
      .500E-03
```
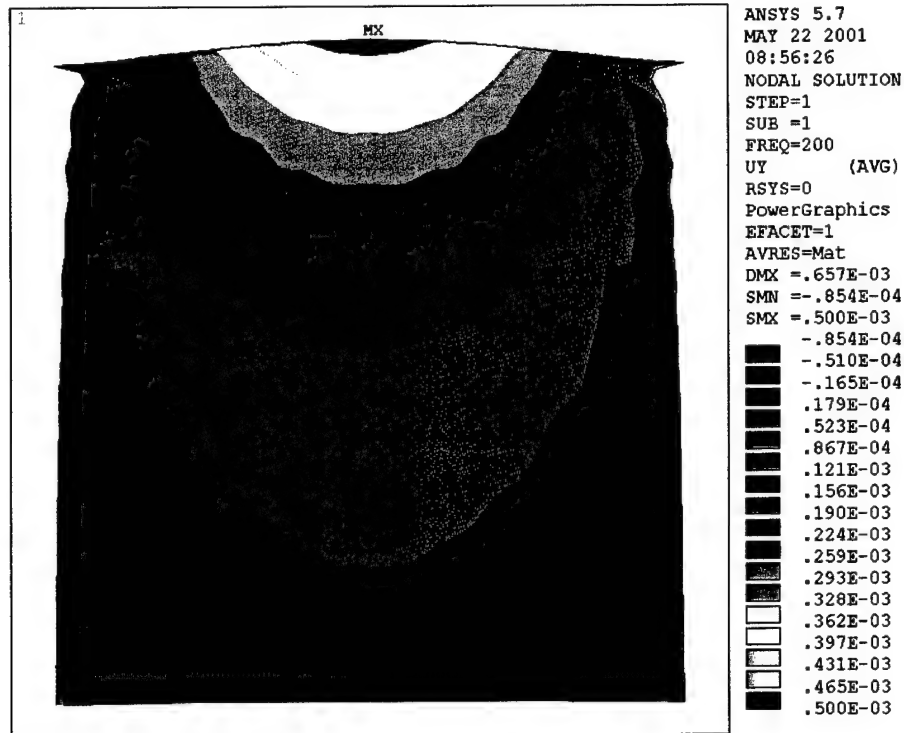
Figure 3. Calculated Longitudinal Displacements for Longitudinal Excitation With Correct Material Properties Using ANSYS.


```
ANSYS 5.7
MAY 24 2001
08:53:46
NODAL SOLUTION
STEP=1
SUB =1
FREQ=200
UX          (AVG)
RSYS=0
PowerGraphics
EFACET=1
AVRES=Mat
DMX =.500E-03
SMN =-.309E-03
SMX =.500E-03
     -.309E-03
     -.262E-03
     -.214E-03
     -.167E-03
     -.119E-03
     -.714E-04
     -.238E-04
      .238E-04
      .714E-04
      .119E-03
      .167E-03
      .214E-03
      .262E-03
      .309E-03
      .357E-03
      .405E-03
      .452E-03
      .500E-03
```
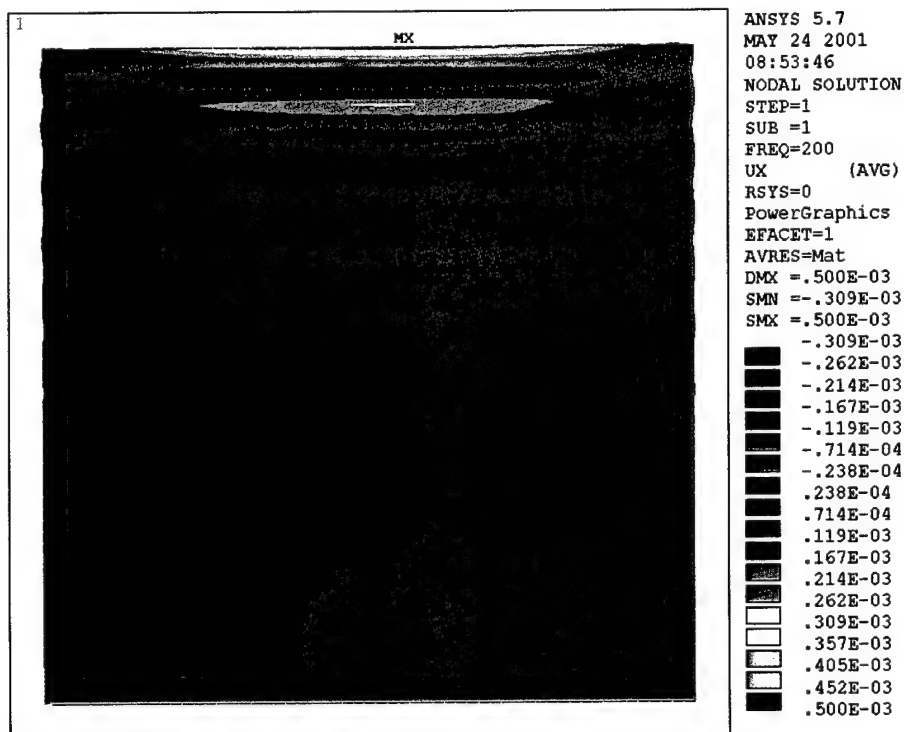
Figure 4. Calculated Shear Displacements for Shear Excitation With Correct Material Properties Using ANSYS.
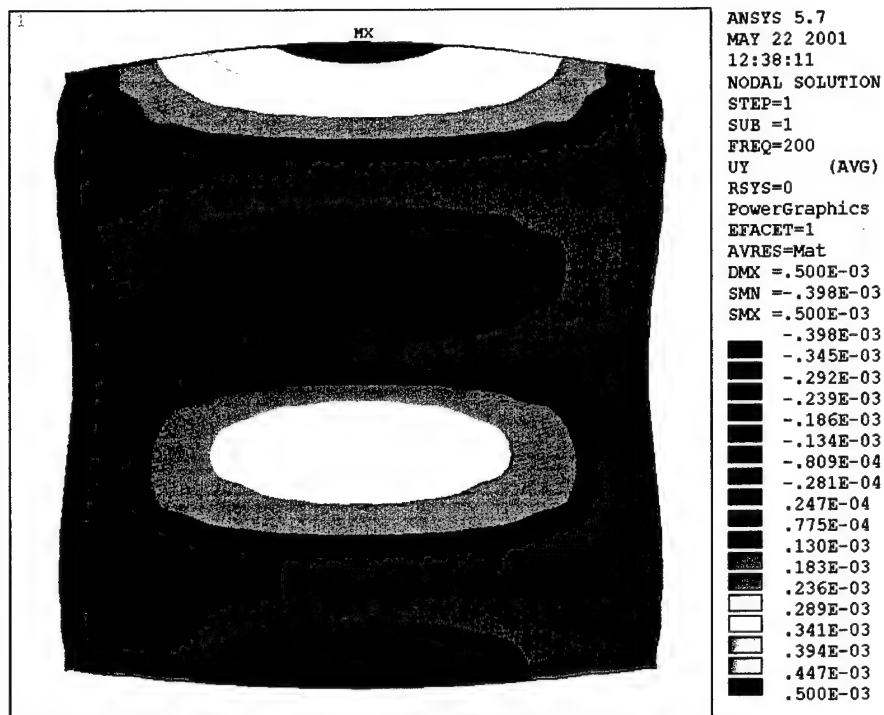
Figure 5. Calculated Longitudinal Displacement for Longitudinal Excitation With Artificially Lowered Poisson's Ratio Using ANSYS.
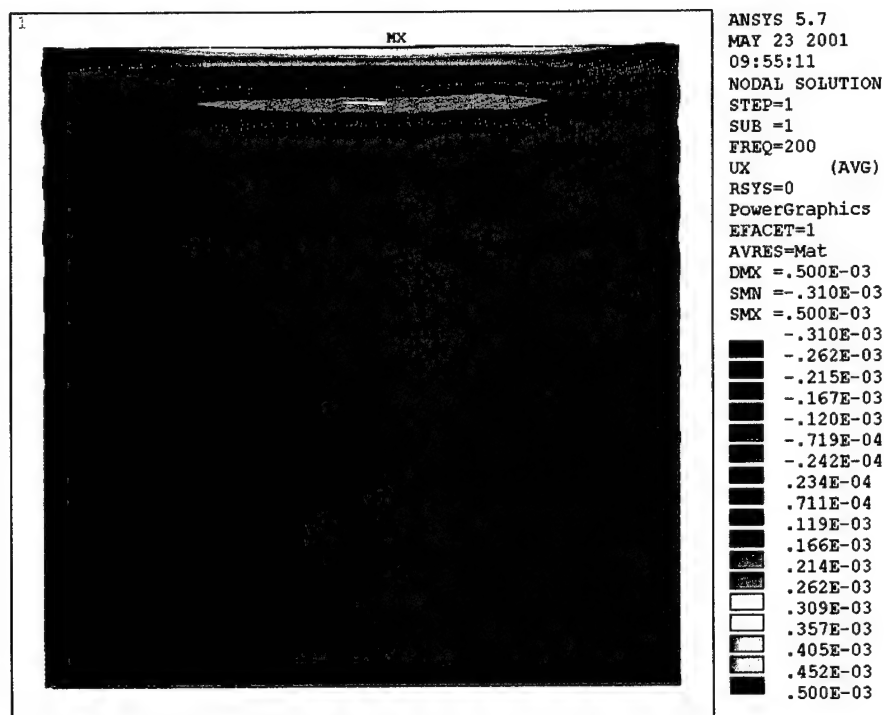
Figure 6. Calculated Shear Displacements for Shear Excitation With Correct Material Properties Using ANSYS with Stiff Inclusion.
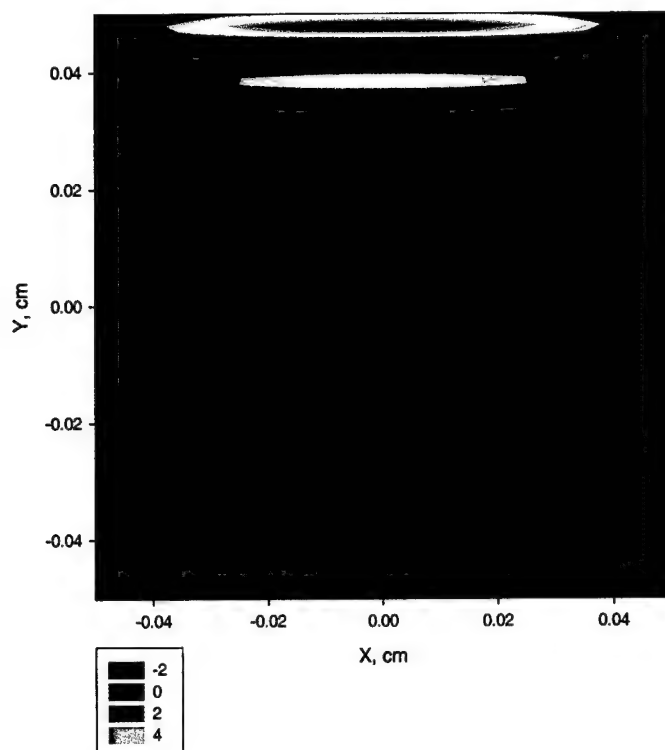
Figure 7. Vorticities Obtained by Differentiating ANSYS-Calculated Displacements for a Homogenous Material (constant stiffness) Excited at 200 Hz.
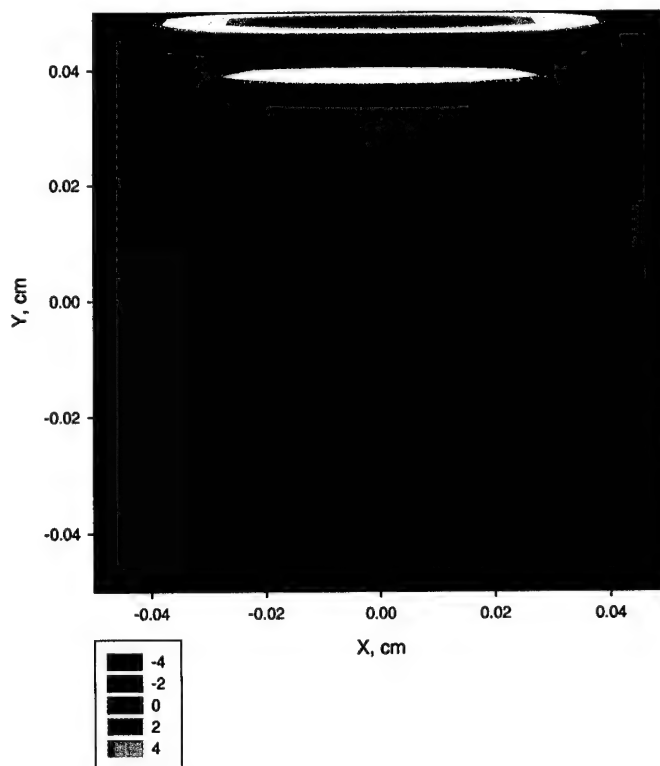
Figure 8. Vorticities Calculated Using Creare Finite Element Code for a Homogeneous Material Excited at 200 Hz.
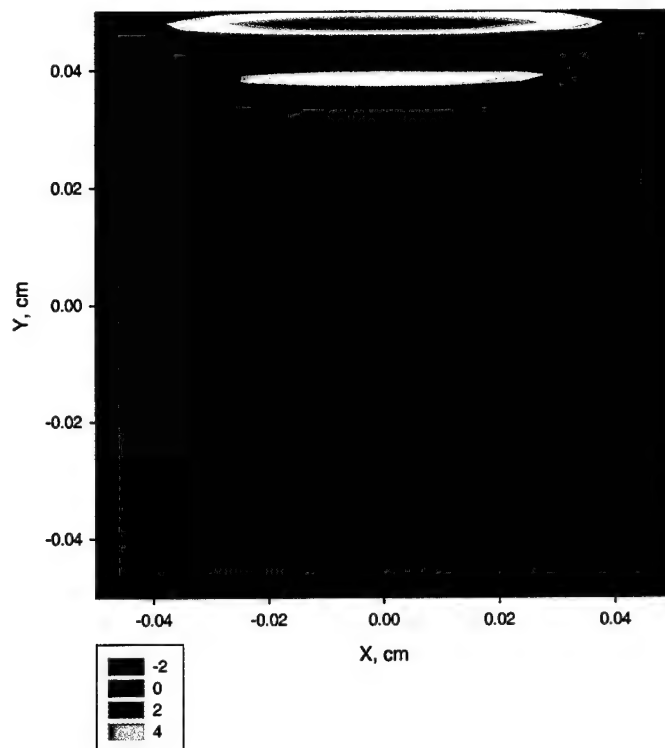
Figure 9. Vorticities Obtained by Differentiating ANSYS-Calculated Displacements for the Case of a Simulated Tumor Imaged at 200 Hz.
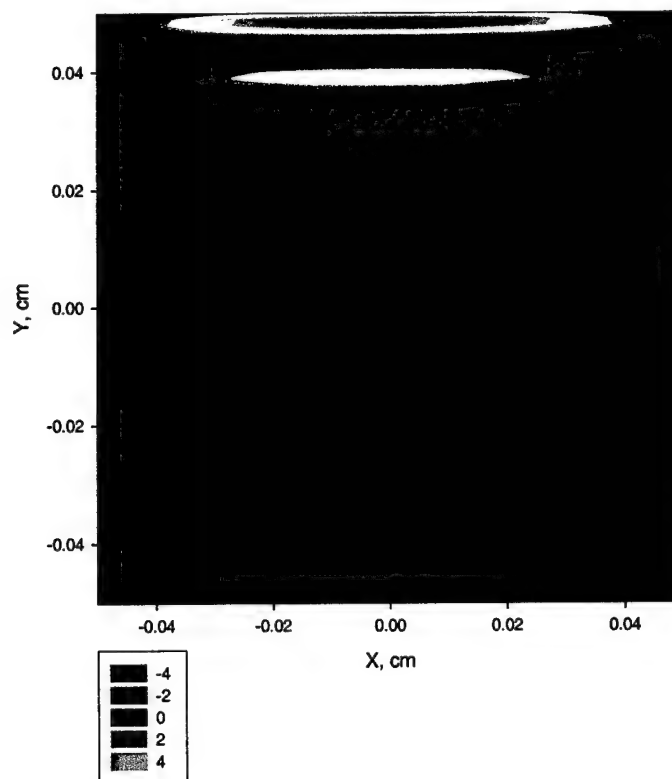
Figure 10. Vorticities Calculated Using Creare Finite Element Code for the Case of a Simulated Tumor Imaged at 200 Hz.
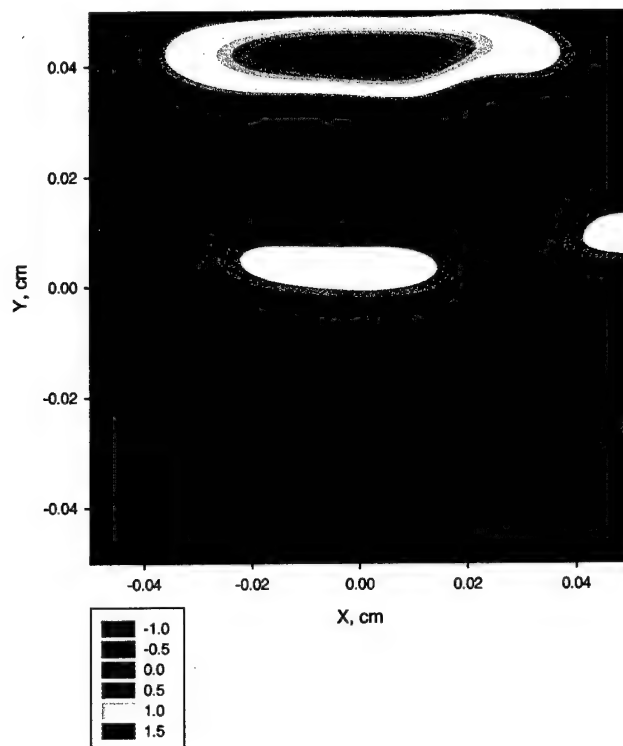
Figure 11. Vorticities Obtained by Differentiating ANSYS-Calculated Displacements for Case With a Simulated Tumor Imaged at 50 Hz.
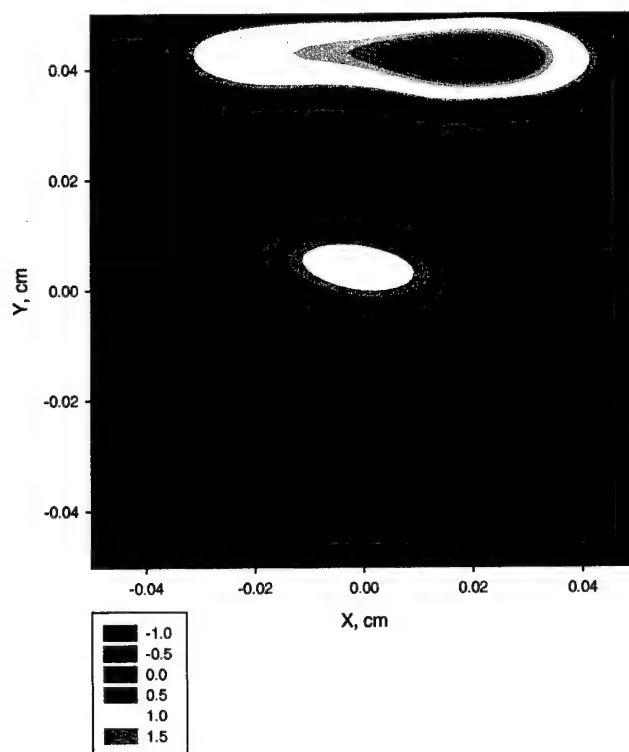
Figure 12. Vorticities Calculated Using Creare Finite Element Code for Case of a Simulated Tumor Imaged at 50 Hz.
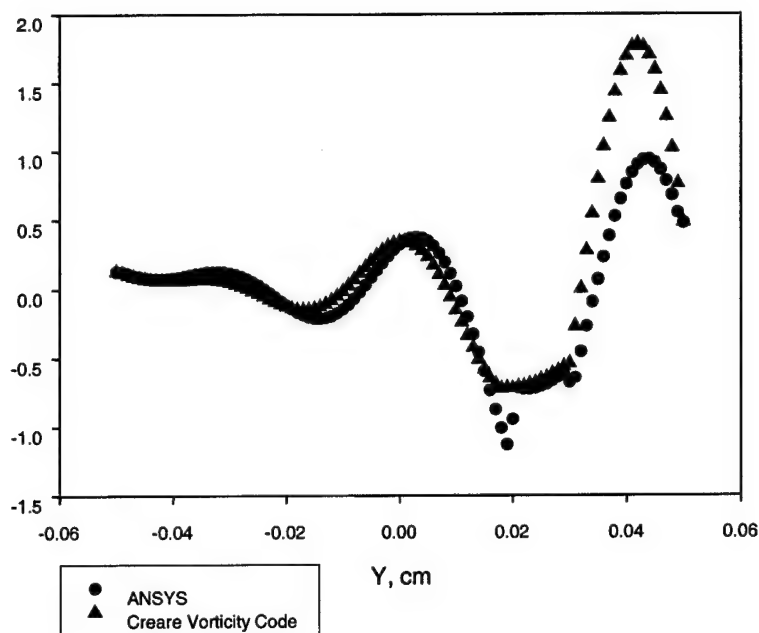
Figure 13. Comparison of Creare and ANSYS Vorticity Values for a Case With a Sharp Discontinuity in Young's Modulus at Tumor Boundaries of y=.02 and .03 cm.
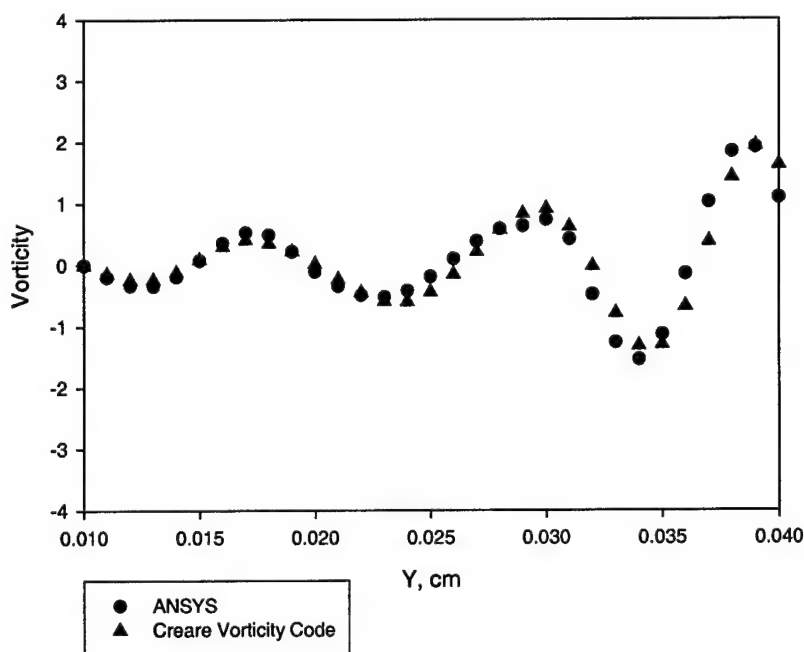
Figure 14. Vorticities for a Case Involving a Tumor With Only Twice the Nominal Stiffness, Imaged at 200 Hz; Little Discontinuity in ANSYS-Calculated Vorticity Is Evident at the Tumor Boundaries of y=.02 and y=.03 cm, and the Two Codes' Results Agree Fairly Well.
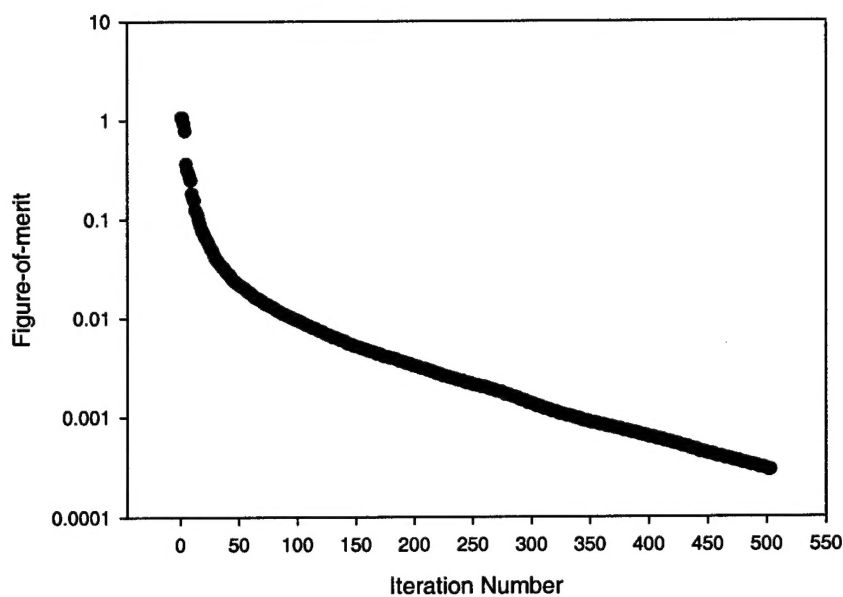
Figure 15. Convergence Rate of BFGS Algorithm. These data show that the figure of merit accuracy improves exponentially (linearly on a log scale) with the number of iterations.
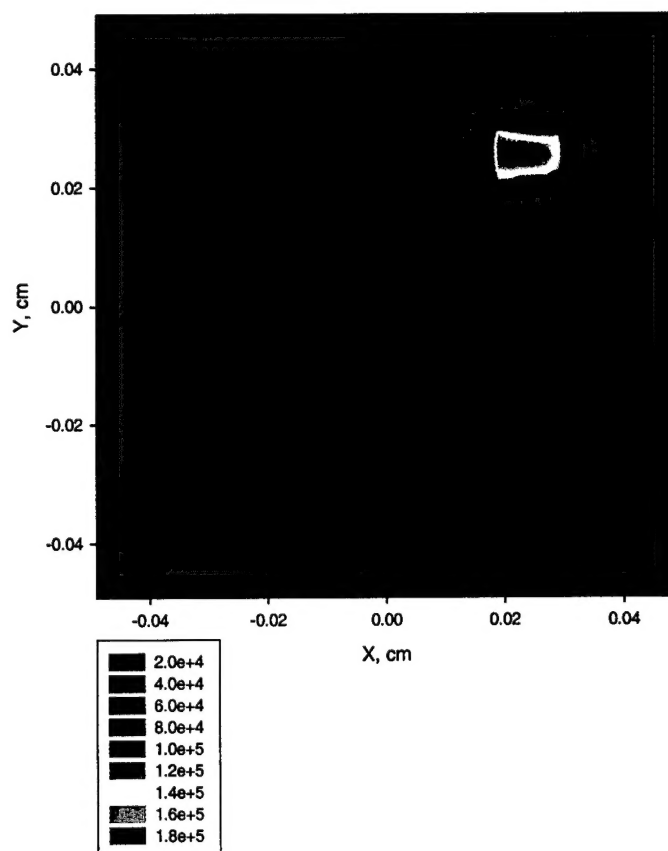

Figure 16. Reconstructed Young's Modulus Using Synthetic Data From Vorticity Model.
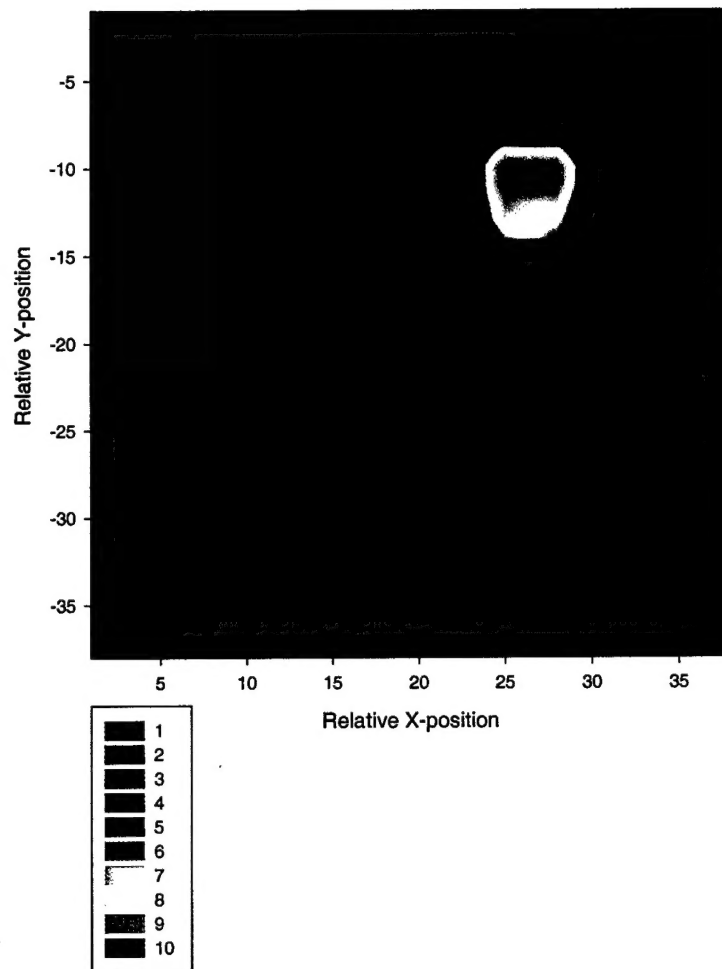
Reconstructed Young's Modulus

Figure 17. Young's Modulus Calculated from Computer-Generated MRI Displacement Data Using the Creare Displacement-Based Code and Inverse Algorithm. The stiffness (relative modulus 10) of the simulated tumor in the upper-right-hand corner can be easily discerned.
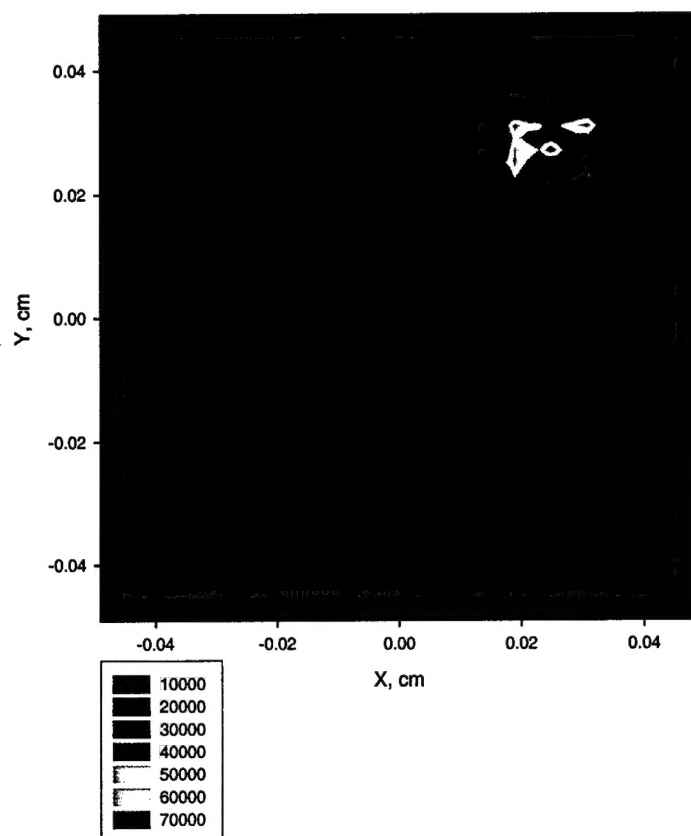
Figure 18. Reconstructed (averaged) Young's Modulus Using Displacement Data From ANSYS Calculation as Input to Vorticity Model. Despite the differences between the two approaches, the presence and location of the tumor are readily apparent

MAGNETIC RESONANCE ELASTOGRAPHY SYSTEM FOR BREAST CANCER DETECTION

Robert J. Kline-Schoder, Ph.D., Marc A. Kenton, Ph.D., and Paul H. Sorensen, Ph.D.

Creare Incorporated
P.O. Box 71, Etna Road; Hanover NH 03755

Rjk@creare.com

One physical characteristic that clearly distinguishes healthy from cancerous tissue is mechanical stiffness (hardness). The Young's modulus of breast tumors can be one to two orders of magnitude larger than that of normal tissue. For this reason, palpation has long been used by physicians and patients for early screening. However, manual palpation is not very effective for tumors lying deep within the breast and is not quantitative. For these reasons, over the past decade, numerous efforts have been underway to combine external mechanical stimulation and various imaging techniques to quantitatively measure the Young's modulus of tissue throughout both the breast and the prostate. This has been termed "palpation at a distance." Because of its inherent sensitivity, much current research is focused on using magnetic resonance imaging (MRI), and the overall process is termed magnetic resonance elastography (MRE).

One of the most challenging technical aspects of MRE is the solution of the "inverse problem," i.e., quantitatively determining Young's modulus from MRI-measured tissue displacement data. Creare is developing analytical solution techniques to improve the efficiency and robustness of the inverse problem solution. We are also investigating improvements in the physical modeling on which the inverse method is based, primarily in the representation of tissue compressibility.

During this project, we have shown: (1) an adjoint method developed on this project provides an extremely efficient technique for calculating the gradient the goodness-of-fit measure that is the basis of the inverse algorithm; (2) combining the adjoint method with a quasi-Newton method, specifically the Boyden-Fletcher-Goldfarb-Shanno (BFGS) algorithm, provides an efficient means for calculating tissue stiffness from MRI displacement data; (3) much of the experience with MRE previously reported in the literature has utilized an incorrect value of Poisson's ratio; and (4) use of an incorrect Poisson's ratio leads to a drastic underprediction of the longitudinal acoustic wavelength, which in turn can be expected to cause artifacts in the reconstructed hardness values.